AIAA SciTech Forum
11–15 & 19–21 January 2021, VIRTUAL EVENT
AIAA Scitech 2021 Forum

10.2514/6.2021-1778

Multidisciplinary Analysis of Propulsive Electric Motors During Takeoff

Tucker Babcock*, Garo Bedonian†, and Jason Hicken‡
Rensselaer Polytechnic Institute, 110 8th St, Troy, NY 12180

The adoption of electric and hybrid-electric propulsion for commercial aircraft has the potential to significantly reduce the aerospace sector's environmental impact. To develop the propulsion systems that meet the critical requirements of these next generation aircraft, new design tools are needed that accurately model the complex coupled electrothermal behavior of electric motors. In this paper we present verification and validation studies for a multidisciplinary electric motor analysis. In particular, we compare to a well studied electromagnetic benchmark problem as well as NASA's X-57 high-lift motor reference design.

I. Introduction

There is growing interest in reducing the greenhouse-gas emissions of aircraft as a means of mitigating the climate impact of air transportation. Among the possible paths to reduced emissions, electric and hybrid-electric propulsion systems are considered compelling options. For example, Brelje and Martins [1] suggest that electric propulsion can help civil aircraft meet the aggressive N+3 performance goals put forth by NASA, which are characterized by stringent emissions, noise, and fuel burn requirements [2].

There are many technical challenges associated with the electrification of aircraft, but the one we focus on here is related to the design of electric motors. Specifically, high current draw during takeoff produces strong Joule heating in the motor's coils and significant waste heating in the motor's core. For example, a trajectory optimization study by Falck et al. [3] predicted that NASA's X-57 would reach thermal constraints during climb. The use of a low-temperature superconducting material for the stator coils has been studied, showing elimination of Joule heating in the windings. However, studies by Brown [4] at NASA on the N3-X propulsion system, and Berg et al. [5] on "cold" superconductor efficiency, have predicted significant power cost incurred by cryogenic cooling. Without cryogenic cooling, it will be necessary to design new motors that account for Joule heating and other waste heat generation during critical operating conditions.

The concerns listed above motivate the use of numerical optimization to produce designs that can meet the requirements of electric aircraft. Weight reduction provides direct improvements to specific power efficiency, while component temperature limits and torque requirements during high-load flight stages (e.g. takeoff) constrain the space of viable designs. To this end, the authors are developing a multidisciplinary shape optimization framework for an air-cooled high-lift motor. This framework will solve a coupled electromagnetic and thermal analysis problem at each design iteration to minimize mass while satisfying performance constraints.

We adopt a high-fidelity approach to modeling the engine, and discretize the relevant partial differential equations using the finite-element method. We first solve a nonlinear electromagnetic problem to compute the electromagnetic performance and electromagnetic losses in the motor. These losses serve as source terms in the heat equation, which models thermal diffusion in the motor, with prescribed boundary conditions to simulate convective cooling on the engine nacelle. The solution to this problem gives the steady-state temperature field in the motor, which can be constrained in an optimization to avoid melting the windings or demagnetizing the permanent magnets.

While the longer-term goal of this work is the development of a full gradient-based optimization, this paper focuses on the implementation and verification of the multi-disciplinary analysis. To that end, we verify the nonlinear electromagnetic solver against the TEAM 13 benchmark problem [6]. We then present simulation results for the full motor, and compare results to results from the NASA X-57 reference motor [7].

The following sections describe the implementation of the forward analysis of air-cooled high-lift electric motors and its verification and validation. Section II introduces the motor's geometry parameterization and presents the relevant physical and mathematical models that describe a motor's electromagnetic and thermal behavior. Section III presents

*Graduate Student, Department of Mechanical, Aerospace, and Nuclear Engineering; Student Member AIAA
†Graduate Student, Department of Mechanical, Aerospace, and Nuclear Engineering; Student Member AIAA
‡Associate Professor, Department of Mechanical, Aerospace, and Nuclear Engineering; Senior Member AIAA

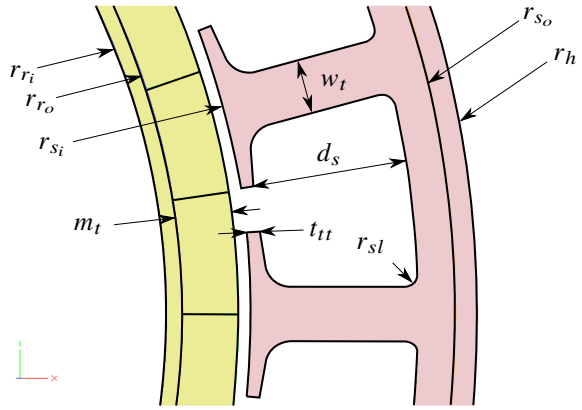

Fig. 1 Diagram showing how design parameters fully define the geometry for the topology of interest.

Table 1 Design parameters and their physical descriptions.

Parameter	Description	Type
n_m	Number of magnets	Discrete
n_s	Number of slots/windings	Discrete
t_l	Lamination thickness	Discrete
l_s	Stack length	Discrete
r_{s_o}	Stator outer radius	Continuous
r_{s_i}	Stator inner radius	Continuous
r_{r_o}	Rotor outer radius	Continuous
r_{r_i}	Rotor inner radius	Continuous
d_s	Slot depth	Continuous
w_t	Tooth width	Continuous
t_m	Magnet thickness	Continuous
r_h	Heat sink outer radius	Continuous
t_{tt}	Tooth tip thickness	Continuous
a_{tt}	Tooth tip angle	Continuous
r_{sl}	Slot radius	Continuous

the finite-element discretization of the electromagnetic and thermal models detailed in Section II. Section IV presents results from the verification and validation studies. Finally, Section V discusses the presented studies and highlights future areas of research.

II. Motor Modeling and Parameterization

This section describes the fundamental physical and design assumptions that motivate the models chosen for the optimization framework. We also address the parameterization adopted for the motor geometry.

A. Geometry Parameterization

While there are a variety of configurations that an electric motor in an aerospace application could be based on, in this work we assume a three-phase brushless direct current (BLDC) permanent magnet motor in which the rotor body exists in the interior of the stator body. We parameterize the BLDC motor geometry using the variables listed in Table 1, and Figure 1 illustrates these parameters. Note that the lamination thickness t_l and the stack length l_s refer to "out-of-the-page" measurements and are not depicted in the diagram. The number of slots, n_s, is equivalent to the number of windings present in the stator; it must be a multiple of the number of phases.

There are other discrete design choices that strongly influence the behavior of the motor. For example, material choices for the different components of the motor can have a significant impact on performance. Another important choice is the magnet pattern, which determines the permanent magnet magnetic field that the stator windings interact with. Different configurations will produce different resultant magnetic fields, which will impact the motor's torque. As we are targeting gradient-based optimization, we cannot account for discrete variables in a single optimization; a parametric sweep with respect to such variables will be required to fully explore the design space, but fast convergence of a gradient-based optimizer should enable such exploration.

B. Electromagnetic Analysis

We model the electromagnetic behavior of the BLDC motor with the magnetostatic approximation of Maxwell's equations, given in differential form by

$$\nabla \times \boldsymbol{H} = \boldsymbol{J}_{\text{src}}, \qquad \forall\, \boldsymbol{x} \in \Omega_E, \tag{1}$$

$$\nabla \cdot \boldsymbol{B} = 0, \qquad \forall\, \boldsymbol{x} \in \Omega_E, \tag{2}$$

where $\boldsymbol{H}$ is the magnetic field intensity, $\boldsymbol{B}$ is the magnetic flux density, and $\boldsymbol{J}_{\text{src}}$ is the applied source current. The set Ω_E denotes the computational domain of the electromagnetic problem, in this case the entire volume of the motor and the air just outside of the motor. Equation (1) is known as Ampère's circuital law, and (2) is known as Gauss's law for magnetism. Boundary conditions are required to make (1) and (2) well posed. These will be discussed shortly.

Although we are modeling a dynamic system such as a motor with a static approximation of Maxwell's equations, this simplifying assumption introduces little error to the problem. When nondimensionalizing Maxwell's equations the nondimensional number $\bar{L}/c\bar{T}$ arises naturally, where $\bar{L}$ is the characteristic length scale, $\bar{T}$ is the characteristic time scale, and c the speed of light. It can be shown that Maxwell's equations reduce to the magnetostatic equations in the limit as $\bar{L}/c\bar{T}$ approaches zero [8]. For an electric motor, with characteristic length based on its diameter and characteristic time scale based on its excitation frequency, it is easy to see that $\bar{L}/c\bar{T}$ is much less than one. This indicates that the magnetic field of an electric motor can safely be assumed to be static.

The magnetic field intensity and magnetic flux density are related through the constitutive relation

$$\boldsymbol{H} = \nu\left(\boldsymbol{B} - \boldsymbol{M}\right), \tag{3}$$

where $\boldsymbol{M}$ is the magnetic flux density created by permanent magnets (the remnant flux density), and ν is the reluctivity. In general, the reluctivity is a material-dependent nonlinear function of the magnetic flux density and temperature. We discuss our implementation of the reluctivity model in Section III.B.

Inspecting (2), we see that it is advantageous to define a magnetic vector potential $\boldsymbol{A}$ such that $\boldsymbol{B} = \nabla \times \boldsymbol{A}$, since then $\nabla \cdot \boldsymbol{B} = \nabla \cdot \nabla \times \boldsymbol{A} = 0$ is automatically satisfied. Furthermore, using this vector potential and the constitutive relation from (3), (1) can be re-written as the following second-order elliptic PDE:

$$\nabla \times (\nu \nabla \times \boldsymbol{A}) - \nabla \times (\nu \boldsymbol{M}) = \boldsymbol{J}_{\text{src}}, \qquad \forall\, \boldsymbol{x} \in \Omega_E. \tag{4}$$

It is straightforward to see that $\boldsymbol{A}$ is non-unique, as the gradient of any scalar function may be added to $\boldsymbol{A}$ without changing the value of $\boldsymbol{B}$. A common approach to remedy this is to impose a gauge condition on $\boldsymbol{A}$, such as the Coulomb gauge, $\nabla \cdot \boldsymbol{A} = 0$. Another is to specify Dirichlet boundary conditions on $\boldsymbol{A}$ along the entire boundary to constrain the solution. Here, we take the second approach, setting the tangential component of $\boldsymbol{A}$ to be zero along the bounding surface, which is equivalent to enforcing that no magnetic flux passes through the surface.

Once the solution to (4) is obtained, secondary field quantities such as $\boldsymbol{B}$ can be computed. The $\boldsymbol{B}$ field will be used to estimate the electromagnetic losses known as core losses using an empirical relation, discussed in detail in Section II.C.

C. Thermal Analysis

The thermal analysis of a BLDC motor is coupled to the electromagnetic analysis as several electromagnetic phenomena act as sources of heat. We model the motor's thermal behavior with the steady-state heat equation, with the divergence of Fourier's law governing thermal diffusion and with source terms added to reflect Joule heating and electromagnetic core losses. The equation is given by

$$-\nabla \cdot (\mathsf{K}\nabla\theta) = \boldsymbol{J}_{\text{src}} \cdot \left(\sigma^{-1}\boldsymbol{J}_{\text{src}}\right) + \rho W_s, \qquad \forall\, \boldsymbol{x} \in \Omega_T, \tag{5}$$

where θ is the temperature, K is the thermal conductivity tensor, σ is the electrical conductivity tensor, $\boldsymbol{J}_{\text{src}}$ is the applied source current from the magnetostatic problem, and ρ is the mass density. The set Ω_T denotes the computational domain of interest for the thermal problem, which is the volume of just the motor. The last term in (5) involves W_s, which is the specific electromagnetic core losses due to hysteresis and eddy-current effects, and is modeled using the empirically derived Steinmetz equation [9],

$$W_s = K_s f^{\alpha} \|\boldsymbol{B}\|^{\beta}, \tag{6}$$

where K_s, α, and β are empirically derived material-dependent constants, $\|\boldsymbol{B}\|$ is the magnitude of the magnetic flux density, and f is the electrical excitation frequency. In general, K and σ are temperature-dependent tensors; however, they are very weak functions of temperature, so we have chosen to model them as temperature-independent. This simplification results in (5) being a linear elliptic PDE in θ.

The only time-varying source in (5) is $\boldsymbol{J}_{\text{src}}$, which, for three-phase BLDC motors, exists in two thirds of the windings at any given time and varies at the characteristic electrical frequency. The time scale associated with the changing current is much smaller than the time scale associated with thermal diffusion, so we model the current source as a time-independent source existing in all windings, equal to the average current in the windings at any given time.

We have chosen boundary conditions that simulate the presence of convective cooling on the exterior of the motor's nacelle. These boundary conditions are in general problem dependent, and will be discussed in more detail for each analyzed design.

III. Numerical Analysis Methods

In this section, we present the discretizations for the electromagnetic and thermal models discussed in Section II. We use the lightweight Modular Finite Element Methods (MFEM) [10] library to implement the finite-element formulations for these analyses. We solve the discrete systems with the linear solvers and preconditioners from the *hypre* library [11]. Furthermore, towards the goal of optimization, we discuss the methods and frameworks we use for geometry representation, mesh generation and mesh movement.

A. Geometry Representation, Mesh Generation, and Movement

The magnetostatic and thermal analyses each require a computational mesh on their domains to solve each respective discretized PDE. We associate each mesh with a parametric CAD model of the motor, so that changes in the design variables are easily translated into geometric changes in the mesh through the CAD system. We define the vector of shape design variables in Table 1 as $\boldsymbol{\alpha} \in \mathbb{R}^n$. We have chosen to use EGADS [12] as the CAD system for its ability to easily generate a finite element mesh on the model using AFLR [13, 14] and Tetgen [15] through the CAPS interface [16], as well as it's capability to provide the sensitivities of the mesh surface nodes with respect to the CAD system's parametric design parameters, $\boldsymbol{\alpha}$ [17].

At each design in an optimization iteration, the mesh must be updated to conform to the current geometry. Rather than regenerate the mesh (which is a non-differentiable operation, in general), we move the mesh based on a linear-elasticity analogy [18], where we consider the problem domain as an elastic solid. Let $\boldsymbol{u}^h \in [V^h]^3$ denote the vector field of mesh node displacements, each component of which is taken from the standard continuous Lagrange finite-element space V^h. Then the mesh-node displacements satisfy the following weak formulation of linear elasticity: find $\boldsymbol{u}^h \in [V^h]^3$ such that

$$\int_\Omega \boldsymbol{\epsilon}^*(\boldsymbol{v}^h) : \boldsymbol{\sigma}^*(\boldsymbol{u}^h) d\Omega = 0, \qquad \forall \boldsymbol{v}^h \in [V^h]^3,$$

where $\boldsymbol{\epsilon}^*$ is the elastic strain tensor and $\boldsymbol{\sigma}^*$ is the stress tensor. There are no forcing terms explicitly in the weak form since we prescribe displacements on every surface. The resulting algebraic linear system can be represented by the following 2×2 block system:

$$\boldsymbol{R}_u(\boldsymbol{u}, \boldsymbol{f}) \equiv \begin{bmatrix} \mathsf{K}_{11} & \mathsf{K}_{12} \\ 0 & \mathsf{I} \end{bmatrix} \begin{bmatrix} \boldsymbol{u}_1 \\ \boldsymbol{u}_2 \end{bmatrix} - \begin{bmatrix} \boldsymbol{0} \\ \boldsymbol{f} \end{bmatrix} = \boldsymbol{0}, \tag{7}$$

where $\boldsymbol{u}_1$ is a vector holding the coefficients to the solution of $\boldsymbol{u}^h$ at the interior mesh nodes, $\boldsymbol{u}_2$ is a vector holding the coefficients to the solution of $\boldsymbol{u}^h$ at the surface mesh nodes, and $\boldsymbol{f}$ represents the prescribed displacement of the boundary nodes.

We solve a modified form of the linear system in (7) for $\boldsymbol{u}_1$ (where the boundary degrees of freedom have been eliminated) using the preconditioned conjugate gradient (PCG) method with an algebraic multigrid (AMG) preconditioner [19] from the *hypre* library. We then update mesh node locations through the relation $\boldsymbol{x} = \boldsymbol{x}_0 + \boldsymbol{u}$, where $\boldsymbol{x}_0 \in \mathbb{R}^{3m}$ denotes the mesh node coordinates for the baseline mesh.

The surface node locations are a function of the shape design variables $\boldsymbol{\alpha}$. We obtain the surface node displacements using the initial locations of the surface nodes $\boldsymbol{x}_\Gamma(\boldsymbol{\alpha}_0)$ through the simple relationship:

$$\boldsymbol{u}_\Gamma(\boldsymbol{\alpha}) \equiv \boldsymbol{x}_\Gamma(\boldsymbol{\alpha}) - \boldsymbol{x}_\Gamma(\boldsymbol{\alpha}_0). \tag{8}$$

In practice, we find $\boldsymbol{x}_\Gamma(\boldsymbol{\alpha})$ by leveraging an EGADS tesselation API that maps the original surface tessellation to a new CAD model.

B. Magnetostatic Discretization

We choose to discretize (4) using the finite-element method with Nédélec's $H(\text{curl})$-conforming vector "edge"-elements [20]. The use of Nédélec elements avoids the spurious solution modes seen when using $H(\text{grad})$ nodal elements to solve electromagnetic problems [21]. These modes occur because the continuity enforced by nodal elements

(both normal and tangential continuity between elements) is non-physical for electromagnetic fields; the magnetic flux density, $\boldsymbol{B}$, may be tangentially discontinuous across an interface, while the magnetic vector potential, $\boldsymbol{A}$, may be normally discontinuous across an interface. Nédélec elements defined in an $H(\text{curl})$-conforming space enforce only tangential continuity between elements, and are thus a natural choice for discretizing the $\boldsymbol{A}$ field. Additionally, if the $\boldsymbol{A}$ field is computed using basis functions defined in the $H(\text{curl})$ function space, the discretely computed curl will be exactly in the kernel of the divergence operator, and Gauss's law for magnetism, (2), will automatically be satisfied in a discrete sense.

At a discrete level, the weak form of (4) is stated as follows: find $\boldsymbol{A}^h \in \delta = \{\boldsymbol{v}^h | \boldsymbol{v}^h \in H(\text{curl})\}$ such that

$$\int_{\Omega_E} \nu \left(\nabla \times \boldsymbol{A}^h\right) \cdot \left(\nabla \times \boldsymbol{w}^h\right) \mathrm{d}\Omega_{\mathrm{E}} - \int_{\Omega_E} \boldsymbol{w}^h \cdot (\nabla \times (\nu \boldsymbol{M}))\, \mathrm{d}\Omega_{\mathrm{E}} - \int_{\Omega_E} \boldsymbol{w}^h \cdot \boldsymbol{J}_{src}\, \mathrm{d}\Omega_{\mathrm{E}} = 0, \tag{9}$$

for all $\boldsymbol{w}^h \in \mathcal{V} = \{\boldsymbol{v}^h | \boldsymbol{v}^h \in H(\text{curl}); \boldsymbol{v}^h = \boldsymbol{0}|_\Gamma\}$ with boundary conditions $\boldsymbol{A}^h \times \boldsymbol{n} = \boldsymbol{0}|_\Gamma$, where, again from Section II.B, Ω_E is the entire volume of the BLDC motor and surrounding air. The resulting algebraic form is given as:

$$\boldsymbol{R}_A = \boldsymbol{R}_A(\boldsymbol{A}, \boldsymbol{x}) = \boldsymbol{0}, \tag{10}$$

where $\boldsymbol{A}$ is a vector holding the coefficients to the solution $\boldsymbol{A}^h$. We solve (10) using Newton's method with a backtracking line search to ensure that each step reduces the L_2 norm of the residual. Each Newton update is computed using the generalized minimum residual method [22] with an auxiliary space AMG preconditioner for $H(\text{curl})$ discretizations [23] from the *hypre* library.

Again, for ferromagnetic materials (iron), the reluctivity ν is a nonlinear function of temperature and magnetic flux density. We use a temperature independent B-spline fit of an experimentally generated B-H curve to define the reluctivity model. The B-spline control points and knot vectors for each material used are listed in the Appendix.

C. Heat Equation Discretization

We again choose the finite-element method to discretize (5), this time with nodal $H(\text{grad})$ finite-elements. For this case, the discrete weak form is stated as follows: find $\theta^h \in \delta = \{v^h | v^h \in H(\text{grad}); v^h = g\,(\boldsymbol{x})|_{\Gamma_D}\}$ such that

$$\int_{\Omega_T} \left(\nabla w^h\right) \cdot \left(\mathsf{K} \nabla \theta^h\right)\, \mathrm{d}\Omega_{\mathrm{T}} - \int_{\Gamma} \left(w^h \mathsf{K} \nabla \theta^h\right) \cdot \boldsymbol{n}\, \mathrm{d}\Gamma - \int_{\Omega_T} w^h \boldsymbol{J}_{src} \cdot \left(\sigma^{-1} \boldsymbol{J}_{src}\right)\, \mathrm{d}\Omega_{\mathrm{T}} - \int_{\Omega_T} w^h \rho W_s\, \mathrm{d}\Omega_{\mathrm{T}} = 0, \tag{11}$$

for all $w^h \in \mathcal{V} = \{v^h | v^h \in H(\text{grad}); v^h = 0|_{\Gamma_D}\}$, where, again from Section II.C, Ω_T is the entire volume of the BLDC motor, and Γ_D is the portion of the boundary with Dirichlet boundary conditions. The algebraic form of this discretization can be written as follows:

$$\boldsymbol{R}_\theta = \boldsymbol{R}_\theta(\boldsymbol{\theta}, \boldsymbol{A}, \boldsymbol{x}) = \boldsymbol{0}. \tag{12}$$

We solve (12) using PCG with the AMG [19] preconditioner from the *hypre* library.

IV. Results

In this section, we present the results of our studies that verify and validate our high-fidelity coupled electric motor analysis.

A. TEAM 13 Benchmark Problem

The TEAM workshop problems serve as benchmarks for numerical analysis codes simulating electromagnetic field problems. Here we present results obtained from solving the TEAM 13 benchmark, which is a nonlinear magnetostatic problem.

The TEAM 13 problem consists of two opposing misaligned steel channels with a thin steel plate inserted between them that creates very small air gaps. A coil excited by a DC current is set between the channels. The current and misalignment of the channels creates a three-dimensional magnetic flux density field. The nonlinear B-H curve for the steel, problem geometry, excitation current, and experimentally obtained values of average magnetic flux density at cross sections in the domain are provided in [24].

The TEAM 13 problem geometry and magnetic flux density field computed with 1000 AT excitation current are shown in Figure 2. The measured and numerically computed average flux densities over several cross sections are

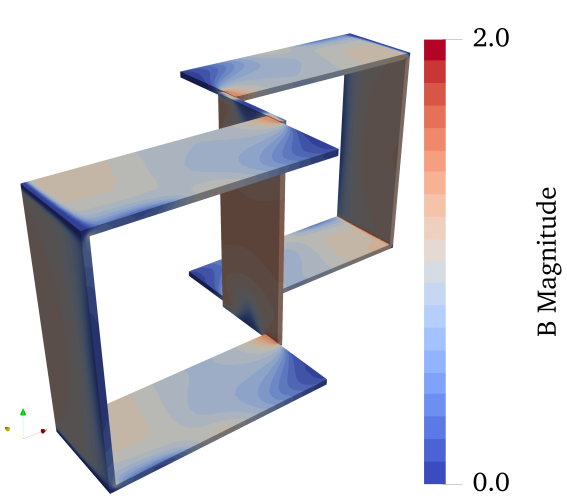

Fig. 2 The calculated magnetic flux density magnitude in the TEAM 13 benchmark geometry.

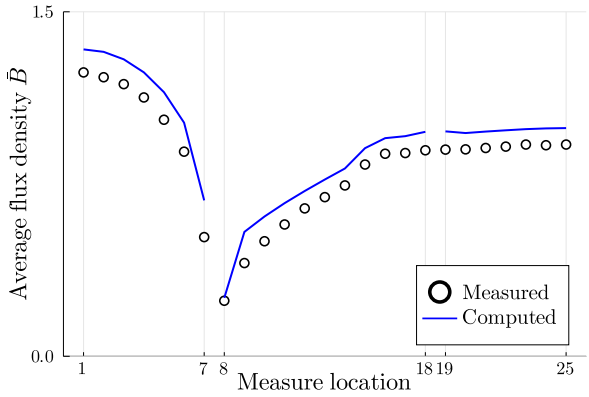

Fig. 3 Average magnetic flux densities from the TEAM 13 benchmark with 1000 AT excitation current across various cross sections from experimental and computational results. Measure locations 1-7 are along the middle plate, 8-18 are along the top of a channel, and 19-25 are along the side of a channel.

plotted in Figure 3, and tabulated in Table 6 in the Appendix. The computed results appear to converge close to but slightly above the measured values. This behavior is consistent with the numerical results from other Nédélec element based codes as reported in [24].

The TEAM benchmark problem presents many of the same challenges to a numerical analysis framework as an electric motor analysis. The small air gaps, high excitation current, and highly saturated steel are present in both problems, and are known to be problematic for numerical routines [25]. The agreement between the experimental and numerical results from the TEAM benchmark suggests that the electromagnetic analysis of the motor will be accurate.

B. X-57 Reference Design

The X-57 reference motor design detailed in [7] included thermal, structural, electromagnetic, and rotordynamic analyses to develop a baseline design for the high-lift motors on NASA's first all-electric X-plane. Here, we reproduce the electromagnetic and thermal results as an additional means of verifying our multidisciplinary analysis framework.

We use the same motor geometry as the reference motor, with design parameters given in Table 2. We also use the same winding layout as the reference design, illustrated in Figure 4. Phases A and B are active at the analyzed design point, with current density 10.7 A/mm^2 and excitation frequency 1000 Hz. The Steinmetz coefficients used for the stator and rotor material, Hiperco 50, have been obtained by curve-fitting material loss data, and are given as $K_s = 0.0044$, $\alpha = 1.286$, and $\beta = 1.76835$. In the absence of available loss data to fit for the $Nd_2Fe_{14}B$ magnets, we have artificially added 15 W of loss in the magnets to match the reference motor. The materials used for the analysis and their relevant thermal properties are listed in Table 3.

For the reference motor analysis we impose Dirichlet temperature boundary conditions on the outer surface of the motor's heat sink and the inner surface of the rotor yoke. These boundary conditions are meant to simulate the presence of convective cooling on the motor's exterior and thus would need to be coupled with a fluid flow analysis on the motor's nacelle to converge to a steady-state temperature. The reference motor design included such an iterative procedure, which is beyond the scope of this work. Here we simply use the steady-state temperatures on the heat sink reported in the X-57 reference motor analysis for the verification of the framework. We include a Dirichlet boundary condition on the inner surface of the rotor yoke because it is thermally connected to the nacelle through its support hardware, as illustrated in Figure 11 from [7]. As we have not modeled this support hardware, we use the steady-state temperature of the rotor yoke reported in the reference design.

We present the results of the maximum temperature computed from our steady-state analysis as well as that from the reference motor paper in Table 4. The table shows good agreement between the reference motor analysis and our own. Figure 5 shows the temperature field across the motor, and Figure 6 shows the magnetic flux density magnitudes in the motor, which qualitatively agree with those in Figure 6 from [7].

Table 2 Design parameters for the X-57 reference motor geometry.

Parameter	Value
n_m	40
n_s	24
t_l	0.1524 mm
l_s	34.5 mm
r_{s_o}	78.225 mm
r_{s_i}	62.25 mm
r_{r_o}	56.85 mm
r_{r_i}	55.625 mm
d_s	12.1 mm
w_t	4.3 mm
t_m	4.4 mm
r_h	80 mm
t_{tt}	1.0 mm
a_{tt}	10.0 degrees
r_{sl}	1.0 mm

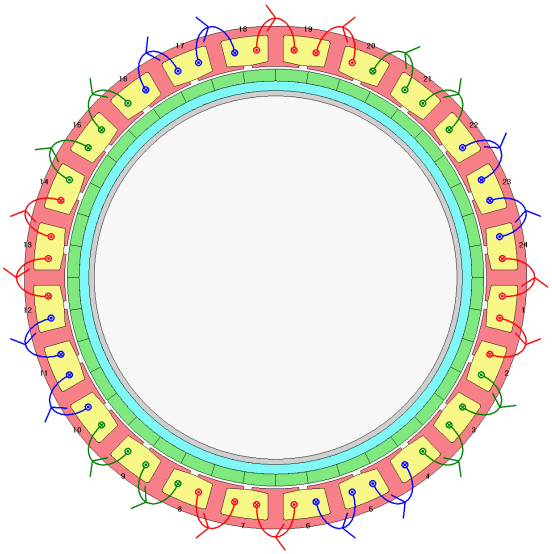

Fig. 4 The winding layout diagram for the X-57 reference motor shows the direction current flows around each tooth. Phases A (blue) and B (red) are active for the analysis.

Table 3 Material properties of materials used for the thermal analysis of the high-lift motor, taken from [7].

Material	Thermal Conductivity (W / mK)	Density (kg / m^3)
2024-T3	120	2780
Hiperco 50	20	8120
$Nd_2Fe_{14}B$	9	7500
Windings (at 59% fill)	2.49	8960

Table 4 The maximum steady-state temperatures calculated with our analysis framework show close alignment to those from [7].

Component	Steady-State Temp (°C)	Reference Steady-State Temp (°C)	Max Allowable Temp (°C)
Stator Windings	133.72	128.65	200
Stator Iron	127.94	127.99	NA
Rotor Magnets	84.30	89.97	120
Rotor Iron	78.29	78.10	NA

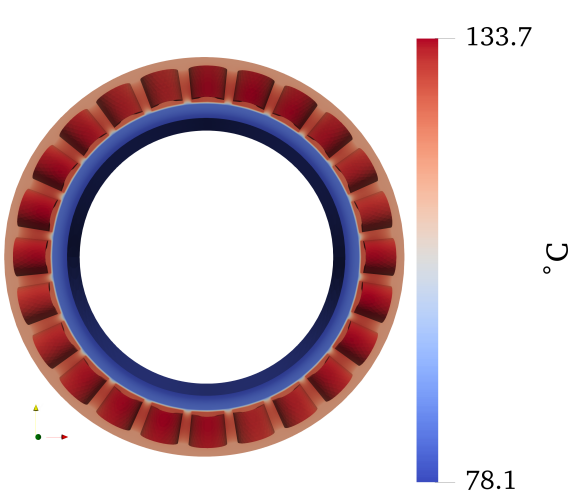

Fig. 5 The temperature distribution over the motor shows that the heat is concentrated near the windings.

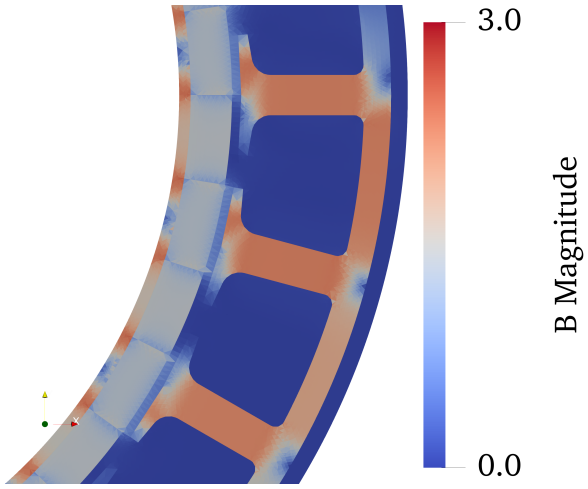

Fig. 6 The magnetic flux density magnitudes in the motor qualitatively agree with those in Figure 6 from [7].

V. Discussion

The goal of this paper has been to describe, verify, and validate a numerical analysis of a coupled electrothermal simulation of electric motors for aircraft. This should be viewed as a stepping stone towards an optimization framework for high-lift electric motors. These motors are constrained by quantities inherent to engineering design: performance requirements and allowable operating conditions (thermal bounds). Due to the complicated physics and coupled behavior of electric motors, the optimal geometry is often non-trivial, making them a great target for numerical optimization.

We have presented the formulation and implementation of the forward analysis of a coupled electrothermal simulation of a high-lift electric motor. We have then verified and validated this analysis by comparing to a common electromagnetic benchmark problem as well as the results gathered from the X-57 reference motor design. Future work and publications will detail the development of a full gradient-based optimization for electric motors, and will investigate the potential for multi-fidelity analysis and optimization.

Appendix

A. B-H Curve Spline Data

We include the control points and knot vector used in our spline fits of the B-H curves for reproducibility. The spline data for the TEAM 13 benchmark material and the reference motor material are given in Table 5. Both fits are extrapolated with the equation

$$H = H_s - \nu_0 B_s + \nu_0 B,$$

where H_s and B_s are the largest values of H and B from the provided data.

B. TEAM 13 Tabulated Results

We tabulate the results for the TEAM 13 benchmark used to generate Figure 3 in Table 6.

Acknowledgments

The authors gratefully acknowledge support for the reported research from the National Aeronautics and Space Administration under the Fellowship Award 20-0091. The authors would like to specifically thank Dustin Hall, Justin Gray and Jeffrey Chin of NASA Glenn Research Center for their advice and input with formulating the motor problem, as well as Bob Haimes and Marshall Galbraith from MIT and Morteza Hakimi from RPI for their time spent helping to generate the meshes used in the analysis.

Table 5 Control points and knot vector for the cubic B-spline fit of the TEAM 13 benchmark material and reference motor material.

TEAM 13 Material		Hiperco 50	
Control Points	Knots	Control Points	Knots
0.0	0.0	0.0	0.0
164.464	0.0	8.99319	0.0
301.355	0.0	10.9783	0.0
161.768	0.0	83.2473	0.0
961.705	0.0979	211.231	1.42459
27015.6	1.3841	458.336	1.8798
138424.0	1.8	1159.13	2.08918
196781.0	2.0	2773.49	2.18485
	2.22	1.3423e6	2.22945
	2.22	2.67533e6	2.26476
	2.22	3.99824e6	2.30288
	2.22		7.290145827
			7.290145827
			7.290145827
			7.290145827
			7.290145827

References

[1] Brelje, B. J., and Martins, J. R., "Electric, hybrid, and turboelectric fixed-wing aircraft: A review of concepts, models, and design approaches," *Progress in Aerospace Sciences*, Vol. 104, 2019, pp. 1 – 19. https://doi.org/https://doi.org/10.1016/j.paerosci.2018.06.004.

[2] Follen, G. J., Del Rosario, R., Wahls, R., and Madavan, N., "NASA's Fundamental Aeronautics Subsonic Fixed Wing Project: Generation N+3 Technology Portfolio," *Aerospace Technology Conference and Exposition*, SAE International, 2011. https://doi.org/https://doi.org/10.4271/2011-01-2521.

[3] Falck, R. D., Chin, J., Schnulo, S. L., Burt, J. M., and Gray, J. S., *Trajectory Optimization of Electric Aircraft Subject to Subsystem Thermal Constraints*, chapter and pages. https://doi.org/10.2514/6.2017-4002.

[4] Brown, G., *Weights and Efficiencies of Electric Components of a Turboelectric Aircraft Propulsion System*, chapter and pages. https://doi.org/10.2514/6.2011-225.

[5] Berg, F., Palmer, J., Miller, P., and Dodds, G., "HTS System and Component Targets for a Distributed Aircraft Propulsion System," *IEEE Transactions on Applied Superconductivity*, Vol. 27, No. 4, 2017, pp. 1–7. https://doi.org/10.1109/TASC.2017.2652319.

[6] The International Compumag Society, "Team Problem 13 3-D Non-Linear Magnetostatic Model," https://www.compumag.org/wp/wp-content/uploads/2018/06/problem13.pdf, 1990. Accessed 25 November 2020.

[7] Hall, D., Chin, J., Anderson, A., Smith, A., Edwards, R., and Duffy, K. P., "Development of a Maxwell X-57 High Lift Motor Reference Design," *AIAA Propulsion and Energy 2019 Forum*, 2019, p. 4481.

[8] Haus, H. A., Melcher, J. R., Zahn, M., and Silva, M., "Electromagnetic Fields and Energy," , Spring 2008. URL https://ocw.mit.edu.

[9] Steinmetz, C. P., "On the law of hysteresis (Part II.) and other phenomena of the magnetic circuit," *Transactions of the American Institute of Electrical Engineers*, Vol. 9, No. 1, 1892, pp. 619–758.

[10] "MFEM: Modular Finite Element Methods Library," mfem.org, 2010. https://doi.org/10.11578/dc.20171025.1248.

[11] Falgout, R. D., and Yang, U. M., "hypre: A library of high performance preconditioners," *International Conference on Computational Science*, Springer, 2002, pp. 632–641.

Table 6 Experimental and numerical average magnetic flux densities at varies measure locations. Experimental results are obtained from [24].

Measure location	Measured	Computed
1.0	1.236	1.33626
2.0	1.215	1.3256
3.0	1.185	1.29306
4.0	1.127	1.23628
5.0	1.03	1.14984
6.0	0.891	1.01716
7.0	0.519	0.678912
8.0	0.242	0.254222
9.0	0.406	0.541694
10.0	0.501	0.608749
11.0	0.574	0.666856
12.0	0.644	0.719744
13.0	0.693	0.769687
14.0	0.744	0.8178
15.0	0.835	0.906287
16.0	0.882	0.949812
17.0	0.885	0.958475
18.0	0.897	0.977425
19.0	0.9	0.979344
20.0	0.901	0.972075
21.0	0.907	0.978519
22.0	0.913	0.984006
23.0	0.922	0.989081
24.0	0.919	0.992287
25.0	0.922	0.993644

[12] Haimes, R., and Drela, M., *On The Construction of Aircraft Conceptual Geometry for High-Fidelity Analysis and Design*, chapter and pages. https://doi.org/10.2514/6.2012-683.

[13] Marcum, D. L., and Weatherill, N. P., "Unstructured grid generation using iterative point insertion and local reconnection," *AIAA journal*, Vol. 33, No. 9, 1995, pp. 1619–1625.

[14] Marcum, D. L., "Unstructured grid generation using automatic point insertion and local reconnection," *The handbook of grid generation*, 1998, pp. 18–1.

[15] Si, H., "TetGen, a Delaunay-based quality tetrahedral mesh generator," *ACM Transactions on Mathematical Software (TOMS)*, Vol. 41, No. 2, 2015, pp. 1–36.

[16] Haimes, R., Dannenhoffer, J., Bhagat, N. D., and Allison, D. L., "Multi-fidelity Geometry-centric Multi-disciplinary Analysis for Design," *AIAA Modeling and Simulation Technologies Conference*, 2016, p. 4007.

[17] Dannenhoffer, J., and Haimes, R., "Design sensitivity calculations directly on CAD-based geometry," *53rd AIAA Aerospace Sciences Meeting*, 2015, p. 1370.

[18] Johnson, A., and Tezduyar, T., "Mesh update strategies in parallel finite element computations of flow problems with moving boundaries and interfaces," *Computer Methods in Applied Mechanics and Engineering*, Vol. 119, No. 1, 1994, pp. 73 – 94. https://doi.org/https://doi.org/10.1016/0045-7825(94)00077-8.

[19] Ruge, J. W., and Stüben, K., "Algebraic multigrid," *Multigrid methods*, SIAM, 1987, pp. 73–130.

[20] Nédélec, J.-C., "Mixed finite elements in $\mathbb{R}^3$," *Numerische Mathematik*, Vol. 35, No. 3, 1980, pp. 315–341.

[21] Sun, D., Manges, J., Yuan, X., and Cendes, Z., "Spurious modes in finite-element methods," *IEEE Antennas and Propagation Magazine*, Vol. 37, No. 5, 1995, pp. 12–24.

[22] Saad, Y., and Schultz, M. H., "GMRES: A generalized minimal residual algorithm for solving nonsymmetric linear systems," *SIAM Journal on scientific and statistical computing*, Vol. 7, No. 3, 1986, pp. 856–869.

[23] Kolev, T. V., and Vassilevski, P. S., "Parallel auxiliary space AMG for H (curl) problems," *Journal of Computational Mathematics*, 2009, pp. 604–623.

[24] Nakata, T., Takahashi, N., and Fujiwara, K., "Summary of results for team workshop problem 13 (3-d nonlinear magnetostatic model)," *COMPEL-The international journal for computation and mathematics in electrical and electronic engineering*, 1995.

[25] Cherif, R., Tang, Z., Guyomarch, F., Chevallier, L., and Le Menach, Y., "An Improved Newton Method Based on Choosing Initial Guess Applied to Scalar Formulation in Nonlinear Magnetostatics," *IEEE Transactions on Magnetics*, Vol. 55, No. 6, 2019, pp. 1–4.